Memoirs of the Faculty of Science, Kyoto University, Series of Physics, Astrophysics, Geophysics and Chemistry, Vol. XXXVI, No. 1, Article 7, 1981

# MEASUREMENT OF THE POLARIZATION PARAMETERS FOR THE $\pi^-p\to\pi^0n$ CHARGE EXCHANGE SCATTERING AT THE MOMENTA OF 2.77, 3.49 AND 4.22 GeV/c

By

**Toshikazu ADACHI**

Department of Physics, Faculty of Science, Kyoto University, Kyoto

*(Received April 5, 1980)*

ABSTRACT

The polarization paremeters for the $\pi^-p\to\pi^0n$ change exchange scattering at three incident pion momenta of 2.77, 3.49 and 4.22 GeV/c have been measured in the $t$ range up to $-2.0$ (GeV/c)$^2$. The results are compared with those of other experiments and the predictions of the partial wave analysis and a Regge model.

## I. Introduction

The high energy behavior of $\pi$N scattering in the forward direction has been studied in terms of Regge pole models since the high energy scattering experiments at CERN and BNL revealed the high energy behavior. For the elastic process $\pi^\pm p\to\pi^\pm p$, both differential cross sections and polarization parameters are well fitted by the $\rho$ and P trajectories. Although the differential cross sections of the charge exchange process $\pi^-p\to\pi^0n$, are also successfully explained in terms of the $\rho$ trajectory, the non zero polarization in the forward direction[1] could not be explained because of the same phase of the real and imaginary parts of the scattering amplitude due to a single trajectory. Many attempts have been made to resolve the problem by considering absorption[2], extra poles besides the $\rho$ pole[3,4] and an additional contrribution from Regge cut[5]. So far, no attempts have succeeded to explain the overall behavior of the polarization data.

In the meantime, the phase shift analyses habe been made by a lot of analyses within last two decades and recently three groups have been carried on for the $\pi$N scattering systematically. Those are Saclay[6], Karlsruhe-Helsinki (K–H 78)[7] and CMU–LBL[8] groups. Last two groups are now in the course of analysing. By those analyses, the $\pi$N scattering amplitudes are fairly well clarified at higher energies and a number of baryon resonances have been established, which are classified successfully in terms of $SU(6)\times O(3)$ classification[9]. However, in the momentum region above 2 GeV/c, there still exist some ambiguities on scattering amplitudes because of a lack of charge exchange scattering data and spin rotation parameters A and R. Therefore, the measurement of differential cross sections and polarization parameters of the charge exchange scattering must be needed to supply the useful informations on the phase shifts.

Under those circumstances, the measurement of polarization parameters for the charge exchange scattering in the t range up to $-2(\mathrm{GeV/c})^2$ has been performed at three momenta 2.77, 3.49 and 4.22 GeV/c. The present measurement has been carried out as the extention of the measurement of cross sections and polarization parameters of the same reaction at almost all angles in the momentum range between 2.0 and 3.0 GeV/c, which had been performed precedingly at KEK as the first experiment with KEK proton synchrotron. Those previous measurements are described in ref. 10 and 11, and those are assigned by 'CEX' measurement, when needed.

In chap. II the experimental procedure is described briefly, since the apparatus and the beam line used in the present measurement were the same as the CEX measurement.

The procedure for the data reduction is described in chap. III.

In chap. IV, the present results of forward polarization parameters are shown and are compared with those of the previous measurements at ANL[13,14]. The comparison with the predictions from K–H 78 analysis and the Regge pole model are also given. Finally, the results of a simple amplitude analysis in terms of the Regge model are discussed. The formulation used in the present analysis are described in Appendix A.

## II. Experimental Procedure

### A. General

The experimental set up is shown in Fig. II–1. The $\pi^-$ beam from an internal Be target of the KEK proton synchrotron was focused on a polarized proton target. The target was surrounded by an assembly of anticounters which detected all charged particles leaving the target and consequently assured no charged particles in the final state. The details of the anticounters are described in ref. 11.

In order to reduce backgrounds from an inelastic scattering and target materials, both energies and directions of two $\gamma$ rays decaying from $\pi^\circ$ meson, and the directions of a neutron were detected. Therefore, two body kinematics for charge exchange scattering was confirmed.

Two $\pi^\circ$ detectors were placed in both sides of the incident beam line and one $\pi^\circ$

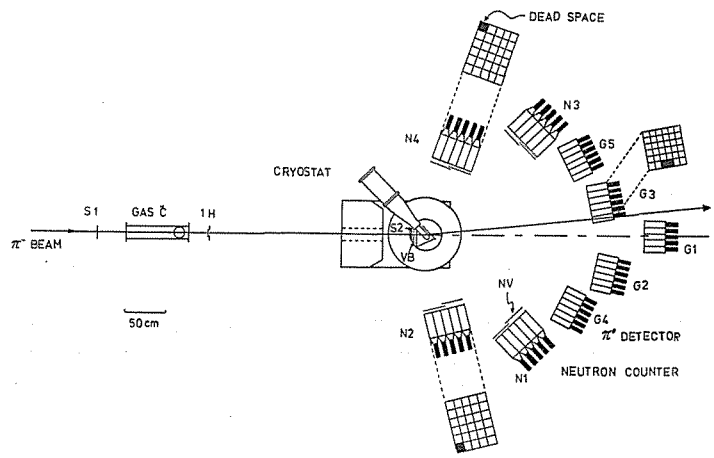


Fig. II–1 A plan view of the apparatus for the present experiment.

detector was placed on the center to increase the acceptance of the detector. Two neutron counter hodoscopes were placed in both sides so that the neutron counter hodoscopes covered the angular region for neutrons satisfying the two body kinematics. Therefore, this counter system formed dual double arms, where the event in which a $\pi^\circ$ meson was scattered in the left hand side and a neutron was recoiled in the right hand side, is denoted as 'left event', and the other case is denoted as 'right event'.

Each $\pi^\circ$ detector and neutron counter hodoscopes consisted of lead glass Cherenkov counters and plastic scintillation counters assembled in matrix, respectively, and is shown in Fig. II–1.

The trigger condition of all detection system is as follows:

(1) $\pi^-$ beam is detected,
(2) no anticounter assembly fires,
(3) more than two lead glass Cherenkov counters fire,
(4) more than one neutron counter fires without no veto counters in front of them firing.

The informations of all the events satisfied above conditions were stored in the PDP 11/40 computer through analog to digital converter (ADC), latches and scalers, and recorded on a magnetic tape. The electronic logic for triggering is shown in Fig. II–2 schematically and details are seen in ref. 11.

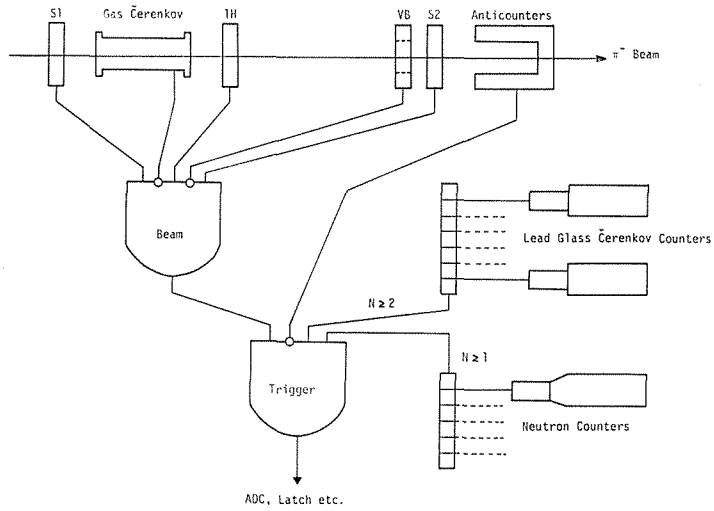


Fig. II–2 A schematic diagram of the logic for the present experiment.

The target polarization was monitored every 17.5 seconds throughout the measurement with the mini computer OKITAC 4300b and was transferred to the PDP 11/40 through CAMAC modules.

At each momentum, the measurements have been performed with the polarized proton target with their spins up and down. The background due to the unpolarized nuclei in the target has been measured with the carbon target contained the same amount of bound protons as in the polarized target. Here, the notation of up (down) is defined so as to be proper in the 'left event'. The same notation is used for the 'right event', although it is not a proper notation.

Thus, polarization parameters were evaluated with the following formula:

$$P(\theta)=\frac{n\uparrow(\theta)-n\downarrow(\theta)}{P\downarrow(n\uparrow(\theta)-C(\theta))+P\uparrow(n\downarrow(\theta)-C(\theta))},$$

where

$P(\theta)$; polarization parameter,

$n\downarrow$ and $n\uparrow$; event rate measured with the target spin up and down,

$C(\theta)$; event rate measured with the carbon target,

$P\downarrow$ and $P\uparrow$; polarization of target protons.

Of course, for the 'right event', the factor of $-1$ must be multiplied to $P(\theta)$ so as to obtain proper polarization parameters. Finally, those polarization parameters for 'left' and 'right' events were averaged.

## B. Beam Line

The circulating protons of KEK synchrotron hit on the internal Be target by multi-traversal mode with repetition rate of about two seconds, and produced the secondary particles at the angle of 10° with respect to the circulating protons. Those particles were extracted to the experimental area through a beam transport system with negative mode.

The beam contained almost negative pions and a few leptons ($\simeq 2\%$ of total particles). The momentum spread of the beam was $\Delta p/p=1\%$, and the beam size was typically 15 mm (FWHM) in the vertical and horizontal directions. The beam pulses were 350 msec long and contained $2\sim 5\times 10^5$ particles per $10^{12}$ circulating protons of 12 GeV.

The momentum of the incident beam was known from the beam optics as a function of magnetic field of the bending magnet of the beam transport system. However, in the present experiment the momentum of the beam was calibrated essentially based on the time of flight (TOF) method.

The schematic diagram of the logic for this calibration is shown in Fig. II–3. The incident beam was defined by the scintillation counters of TOF #1, $S_2$ and TOF #2, and the leptonic contamination was rejected with the gas Cherenkov counter of threshold type.

The procedure is as follows:

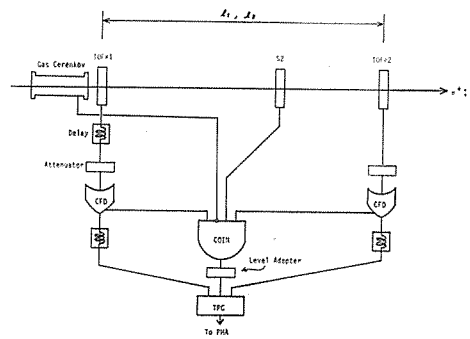


Fig. II–3 A schematic diagram of the logic for the measurement of the beam momentum calibration. The distance between TOF#1 and TOF#2 is about 12 m.

(1) the time of flight of positive pions $T_1$ was measured at the distance of $l_1$,
(2) the time of flight of protons $T_2$ was measured at the distance of $l_2$ by moving the counter TOF #2.

The distance $l_2(l_1 > l_2)$ was adjusted in order that $T_1$ equals to $T_2$ (actually $T_1 \simeq T_2$). Then, the beam momentum was calculated with following formula doing the iterations as follows:

$$\beta_p = (l_2/l_1)(1+(T_1-T_2)/T_2)\beta_\pi$$
$$\downarrow$$
$$P = m\beta_p/\sqrt{1-\beta_p^2}$$
$$\downarrow$$
$$\beta_\pi = P/\sqrt{P^2+\mu^2}$$

where $\beta_\pi(\beta_p)$ denotes the velocity of the pion (proton), $\mu(m)$ denotes the mass of the pion (proton) and $P$ denotes the beam momentum. The advantage of this method is that the measuring system required the linear region not to be in full channel but only in the channel region of $T_1$ and $T_2$.

In order to assure the time stabilily, a constant fraction discriminator (CFD) was used. The time of flight was converted to pulse height with a time to pulse height converter (TPC) and recorded with a pulse height analyser (PHA). The overall stability of this system was about $10^{-4}$ and the resolutions of the time of flight spectrum for protons and pions were about 400 psec in FWHM. The typical PHA spectrum of pions and protons are shown in Fig. II–4.

As the result, the beam momentum at nominal value 2.0 GeV/c was $1.964 \pm 0.004$ GeV/c. Finally, the correction factor $R$ was determined to be the following value:

$$R = 1.964/2.0 = 0.982$$

This correction factor was also used for higher momenta. The results are listed in table II–1.

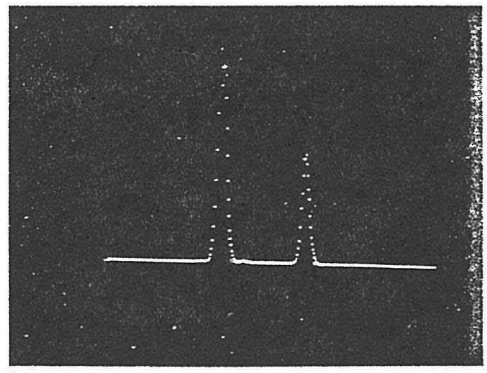

Fig. II–4 Typical time of flight spectrum of pions and protons displayed on the screen of the PHA. The higher signal corresponds to $\pi^-$ mesons and the other signal corresponds to protons. A relative time difference is about 4nsec.

Table II-1. Nominal and calibrated momenta of the beam are listed together with the voltages of the bending magnet D2. The calibrated value are at the exit of the final bending magnet D4, therefore, an actual momentum at the target point must be evaluated taking into account of the energy loss due to materials in the beam line.

| Momentum (MeV/c) | | D2 Magnet (V) |
|---|---|---|
| Nominal | Calibrated | |
| 2000 | 1975 | 3.710 |
| 2100 | 2076 | 3.896 |
| 2200 | 2178 | 4.086 |
| 2300 | 2276 | 4.267 |
| 2400 | 2376 | 4.452 |
| 2500 | 2476 | 4.638 |
| 2600 | 2575 | 4.823 |
| 2700 | 2675 | 5.009 |
| 2800 | 2774 | 5.194 |
| 2900 | 2872 | 5.380 |
| 3000 | 2970 | 5.565 |
| 3500 | 3493 | 6.576 |
| 4250 | 4225 | 8.096 |

## C. Polarized Proton Target

The polarized proton target was cooled down below a temperature of 0.5°K with a $He^3$ cryostat, which was developed by the KEK target group. The target was installed at the center of the polarizing magnet with the uniform field of 2.5 T.

The target material was made of ethylene glycol doped with $Cr^v$ ions and was formed into green beads of about 1 mm$\phi$. The target container, which was made of teflon sheet, was installed in a micro wave cavity. The dimension of the cavity was 88 mm long, 26 mm high and 30.9 mm wide.

The dynamic polarization of free protons in the target induced by a spin-spin coupling between electrons and protons in terms of micro wave of a frequency around 70 GHz was measured with Q-meter method described below.

When the target material, which is put in the external magnetic field, suffers circulating magnetic field on the plane perpendicular to the external field induced with an appropriate coil, the material has a transverse magnetization to change the impedance of the LC circuit. This change of the impedance is measured as a nuclear magnetic resonance (NMR) signal. Therefore, the target polarization can be evaluated with the following formula:

$$P = SP_0/S_0,$$

where $P$ denotes the target polarization induced by dynamic polarization, $S$ denotes the integrated NMR signal (enhanced signal) and $S_0$ denotes the intergrated signal when no micro wave is applied (natural signal). $P_0$ is the target polarization without micro wave, which can be evaluated in terms of the Boltzmann distribution at the known temperature ($T$) as follows:

$$P_0 = (1 - \mathrm{EXP}(-h\nu/kT))/(1 + \mathrm{EXP}(-h\nu/kT)) = \tanh(h\nu/2kT)$$

(in this case, $\nu = 105.8$ MHz and $T \simeq 0.7$°K).

The NMR signal was received with a device of superheterodyne type and was conpensated with an analog conpensator which canceled the smooth background signal. The OKITAC 4300b was used to control an NMR monitor system. The details of control program are described in Appendix B. The radio frequencies of an NMR signal were modulated with a nine bits digital to analog converter (DAC) in the frequency range of 1 MHz. The NMR signal output through the conpensater was analysed with a twelve bits bi-polar ADC and stored into memories of the computer. The data of the NMR signal consisted of 512 channels which corresponded to steps of modulation.

The natural signal was measured with the following procedure.

(1) An NMR signal was measured under the appropriate resonance condition of magnetic field and radio frequencies (signal 1).
(2) Next, the magnetic field was changed slightly not so as to resonate, and only background signal was measured (signal 2).
(3) The natural signal was obtained by subtracting signal 2 from signal 1.
(4) Finally, the background was evaluated by fitting with quadratic polynomials at both sides of natural signal except NMR signal region.

Then the pure NMR signal was obtained by interpolating the polynomial into the signal region.

The deviation of this fitting procedure was estimated to be 4% of intergrated signal. The enhanced signal caused from dynamic polarization was measured with the same procedure except step (2) because of the relative small background signal. The deviation was 3% of integrated signal. Therefore, an error arising from the measurement of the target polarization was evaluated to be 5%.

The natural signals were measured beforehand of every machine cycle, and recorded on a paper tape. During the target up (down) run, the target polarization was evaluated by using an averaged natural signal and $P_0$, and transferred to PDP 11/40 every 17.5 sec. The averaged target polarization of about 65% was achieved during the measurement.

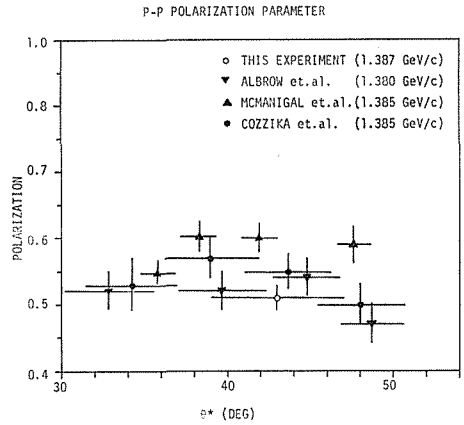


Fig. II–5. Results obtained from the measurement of the polarization parameter for pp elastic scattering and the previous data measured at other laboratories, where ○ denotes the present data, ▼ denotes the data of Alblow et al. and ● denotes the data of Cozzika et. al[16].

Since the Q-meter method measured the polarization of target protons only inside the volume of the detection coil, overall polarization could not be measured. There was possibility that the inhomogeneity of the polarization in the overall target arised from an inhomogeneous distribution of temperature and power of micro wave. In order to test the polarization measurement of the Q-meter method, an independent measurement of the polarization parameter for pp elastic scattering at the momentum of 1.387 GeV/c was performed at the center of mass angle of 43° with the same polarized proton target system. In this measurement, directions of scattered particles and recoiled particles were detected with two sets of four layers of multi-wired spark chambers placed at both sides of the beam line. Since the positive beam from the beam transport system included protons and $\pi^+$ mesons, an identification of particles was made by measuring the time of flight of both particles. The protons and $\pi^+$ mesons were clearly separated. Background events arising from bound protons in heavy nuclei were subtracted by measuring the yield from the carbon target which contained the same amount of bound protons as in the polarized proton target. As is shown in Fig. II–5, the resutls are in good agreement with the previous measurement[12].

## D. Detection System

### D–1 Detectors

A $\pi^\circ$ detection system consisted of five boxes, and each $\pi^\circ$ detector was made of 30 or 36 lead glass Cherenkov counters assembled in $5\times6$ (G ♯1) or $6\times6$ (G ♯2$\sim$5) matrix. A lead glass Cherenkov counter was made of SF6N lead glass of 75 mm wide, 75 mm high and 235 mm long (14 radiation lengths) viewed by HTV R329P photo tube. The energy gain and resolution of the lead glass Cherenkov counters are described in details in ref. 10. Set up parameters are listed in Table II–2(a).

Neutron counter hodoscopes consisted of four boxes, and each box was made of

Table II–2 (a). Set up parameters for $\pi^\circ$ detectors
$R$ denotes the distance between the target point and the face of each detector. $\theta$ denotes the polar angle with respect to the incident beam line, where negative values correspond to the angle of detectors placed at right hand side. Bias is the minimum acceptable energy deposited in the detector.

| BOX | $R$ (cm) | $\theta$ (deg) | Bias (MeV) |
|---|---|---|---|
| G♯ 1 | 271.4 | 0.4 | 200 |
| 2 | 207.0 | −11.7 | 227 |
| 3 | 198.6 | 11.2 | 142 |
| 4 | 179.7 | −26.2 | 142 |
| 5 | 181.9 | 26.8 | 142 |

Table II–2 (b). Set up parameters for neutron counter hoscopes
Meanings of $R$, $\theta$ and bias are the same as in the table II–2 (a).

| BOX | $R$ (cm) | $\theta$ (deg) | Bias (MeV) |
|---|---|---|---|
| N♯ 1 | 149.9 | −46.8 | 20 |
| 2 | 90.9 | −75.4 | 20 |
| 3 | 157.7 | 44.6 | 20 |
| 4 | 92.1 | 69.7 | 20 |

30 plastic scintillaters assembled in 5 × 6 matrix (N #1 ~ 4). A dimension of the plastic scintillater was 100 mm high, 100 mm wide and 300 mm long and viewed by NTV R329P photo tube through a lucite light guide. An anticounter was placed in front of each box in order to reject charged particles which had not been detected by the anticounter assembly surrounding the target. The characteristics of the neutron counters are given in ref. 11 in details. Set up parameters are listed in Table II–2(b).

### D–2 Determination of the position of the decay $\gamma$ rays

In order to determine the energy and direction of the $\pi^\circ$ meson with good precision, both positions hitted by two $\gamma$ rays decaying from $\pi^\circ$ meson must be determined as precisely as possible. In the present experiment, the position of the decay $\gamma$ ray was determined as follows.

The $\gamma$ ray in the lead glass counter produces a shower, and a portion of the shower leaks into neighbouring lead glass depending on the incident position of the $\gamma$ ray. This feature is shown in Fig. II–6 schematically. This position dependence can be expressed with the following empirical relation in terms of the horizontal and vertical displacement $X$ and $Y$ from the counter center $(X_0, Y_0)$:

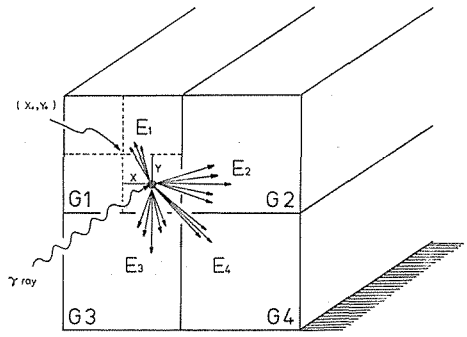


Fig. II–6 A schematic view of the position determination of the incident $\gamma$ ray. In the present case, the incident $\gamma$ ray enters the glass unit $G_1$ at $(X_0+X, Y_0+Y)$, and produces a shower. A portion of the shower leaks into the neighbouring glass units $G_2$, $G_3$ and $G_4$. $E_1$, $E_2$, $E_3$ and $E_4$ denote the pulse heights at each glass unit, respectively.

$$E_X/E_0 = 0.034 \cdot \mathrm{EXP}\,(0.00176 \cdot X^2)$$
$$E_Y/E_0 = 0.034 \cdot \mathrm{EXP}\,(0.00176 \cdot Y^2),$$

or equivalently,

$$X = \sqrt{\log\,(E_x/E_0/0.034)/0.00176}$$
$$Y = \sqrt{\log\,(E_Y/E_0/0.034)/0.00176},$$

where $E_X$ and $E_Y$ are the amount of the leak energies in the $X$ and $Y$ direction, respectively. $E_0$ denotes the total energy of the $\gamma$ ray. For the case shown in Fig. II–6; $E_0 = \sum_{i=1}^{4} E_i$, $E_X = E_2$ and $E_Y = E_3$. Numerical parameters were determined with the calibration measurement for lead glass counters.

The reliability of this method was tested with the data measured in the CEX

experiment. Since the combination of the lead plate converter and the multi-wired spark chambers (MWSC) were used in the CEX experiment, the position of the $\gamma$ ray was determined with the accuracy of $\pm 13$ mm. From the data at the momenta of 2.8 and 3.0 GeV/c of the CEX experiment the position of the $\gamma$ ray could be determined from the MWSC data which is denoted as $(X_w, Y_w)$. From the same data the position of the $\gamma$ ray was also evaluated by the above method without the MWSC data, which is denoted as $(X_0+X, Y_0+Y)$. These two values of the position were compared as follows:

$$(\Delta X_1, \Delta Y_1)=(X_w-(X_0+X), Y_w-(Y_0+Y))$$
$$(\Delta X_2, \Delta Y_2)=(X_w-X_0, Y_w-Y_0).$$

The second equation represents the deviation of the position of the $\gamma$ ray when the position is regarded as a center of the lead glass counter. Consequently, this deviation represents the actual distribution of the $\gamma$ ray position of the lead glass counters, are shown in Fig. II–7. In this figure the solid line represents $\Delta X_1$ or $\Delta Y_1$ and the dashed line represents $\Delta X_2$ or $\Delta Y_2$. As the result, the present method can evaluate the $\gamma$ ray position with the accuracy of $\pm 15$ mm.

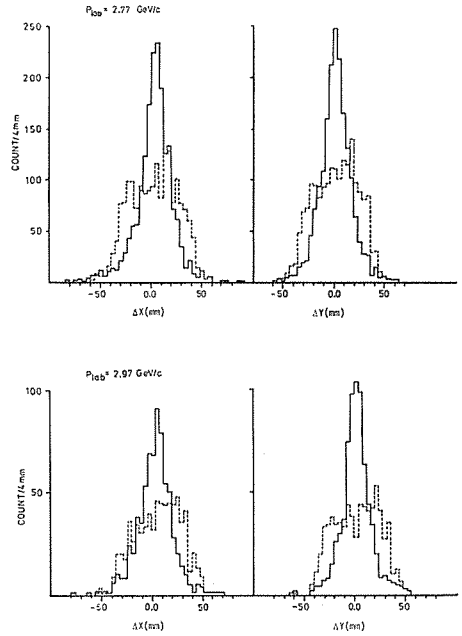


Fig. II–7 A distribution of the deviation of the hitting of $\gamma$ rays. Solid histogram shows the deviation of $\gamma$ ray position corrected by the method described in the text. Dashed histogram shows the distribution of $\gamma$ ray hitting position on the surface of the lead glass.

## III. Data Reduction

### A. General

The data were collected for the incident momenta of 2.770, 3.490 and 4.220 GeV/c consuming about 300 hours of the machine time including the calibration of

counters and other check of the detection system. Total amount of beam and the number of events collected throughout the measurement are listed in Table III–1.

The information on each event contained the pulse height for lead glass Cherenkov counters and hodoscope numbers, contents of many scalers and the target polarization. These informations were condensed into 544 bytes in the PDP 11/40 computer. Finally, the informations were recorded on a magnetic tape with the density of 800 bpi. These magnetic tapes of raw data amounted to 53 rolls in the present measurement. With the KEK central computer HITAC 8800, the raw data were selected under the condition that energies of both $\gamma$ rays must be higher than 200 MeV, and were transferred on a magnetic tape with the density of 1600 bpi. These edited magnetic tapes amounted to 9 rolls and were used throughout the following event processing.

Table III–1. Total numbers of the beam and trigger events.

| Momentum | Target | Beam | Two $\gamma$ Trigger |
|---|---|---|---|
| 2.770 GeV/c | UP | $10672\times10^6$ | 180843 |
| | DOWN | 11315 | 177663 |
| | CARBON | 9115 | 117906 |
| 3.490 GeV/c | UP | 12448 | 210199 |
| | DOWN | 12891 | 226130 |
| | CARBON | 9177 | 121211 |
| 4.220 GeV/c | UP | 11741 | 222543 |
| | DOWN | 13935 | 245112 |
| | CARBON | 13479 | 181918 |

## B. Event Processing

The procedure of the event processing has been performed with the following six steps.

(1) At first the events in which two $\gamma$ rays hit the adjacent two Cherenkov counters were rejected. Then the events were selected with the condition that the energies of both $\gamma$ rays must be higher than 250 MeV. About 20% of total events were selected through this selection.

(2) Since the trigger condition did not contain the identification of the 'left event' and the 'right event', there were many wrong triggered events arised from an inelastic scattering. Therefore, only the events disatisfied the criteria, in which the $\pi^\circ$ meson and the neutron emitted in opposit direction with respect to the beam line, were rejected. The wrong triggered events amounted to about 20% of selected events through the step (1).

(3) The invariant mass $\mu$ of two $\gamma$ rays were evaluated with the following formula:

$$\mu^2=2k_1k_2(1-\cos\phi),$$

where $k_1$ and $k_2$ are energies of two $\gamma$ rays. $\phi$ is an opening angle of two $\gamma$ rays. In order to evaluate $\phi$, the hitting points of $\gamma$ rays were estimated with the method described in section II–D–2. The decaying point of $\pi^\circ$ meson was assumed to be the target center. Supposing that the origin of two $\gamma$ rays are $\pi^\circ$ meson, the energies of two $\gamma$ rays are reconstructed in order to satisfy the decay kinematics of $\pi^\circ\to\gamma\gamma$ by minimizing the following $\chi^2$ [15]:

$$\chi^2=\sum_{i=1}^{2}(k_i-k_i^0)^2/\sigma_i^2$$
$$\sigma_i=\alpha_i\sqrt{k_i^0},$$

where $k_i^0$ denotes the most probable energy and $\alpha_i$ denotes the coefficient related to the energy resolution of the lead glass counters which had been determined from the calibration measurement. Consequently, $k_i^0$ is expressed by

$$k_1^0=\sqrt{(\alpha_2^2k_1^1+\alpha_1^2A)/(\alpha_2^2+\alpha_1^2k_2^2/A)},$$
$$k_2^0=A/k_1^0,$$
$$A=\mu_0^2/2\,(1-\cos\phi),$$

where $\mu_0$ denotes the $\pi^\circ$ mass.
$\chi^2$ is the measure of the deviation from the true $\pi^\circ$ event. The candidates of $\pi^\circ$ events were selected by rejecting the large $\chi^2$ events ($\chi^2>10$). This cut corresponds to the region of the invariant mass of $50<\mu<200$ MeV. The typical invariant mass distribution is shown in Fig. III–1. In this process, about 20% of selected events were rejected.

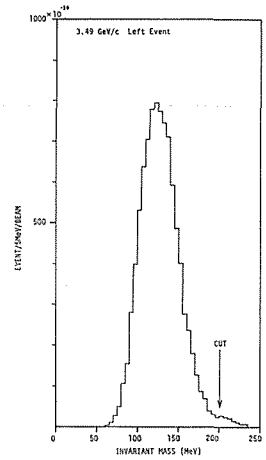


Fig. III–1 A typical invariant mass distribution of the two $\gamma$ rays for the left event at the momentum of 3.49 GeV/c.

(4) By using $k^0$'s evaluated in the step (3) and the direction of two $\gamma$ rays, the momentum of $\pi^\circ$ meson and the scattering angle $\theta$ were evaluated for each event. The momentum and angle of $\pi^\circ$ meson thus obtained were tested with the two body kinematics of charge exchange scattering. The deviation of the laboratory momentum $\Delta P$ is defined as follows:

$$\Delta P=(P_L-P_L^0(\cos\theta))/\sigma_P$$
$$\sigma_P=\sqrt{(\alpha_1k_1^0)^2+(\alpha_2k_2^0)^2},$$

where $P_L$ denotes the measured momentum of $\pi^\circ$ meson, $P_L^0(\cos\theta)$ denotes the momentum evaluated kinematically with the measured angle $\theta$. There-

fore, $\Delta P$ is the measure of the kinematical test between $\theta$ and $P_L$. As is shown in Fig. III–2, the $\Delta P$ distribution has the tail in the negative region. This tail less than $\Delta P=-2$ was rejected.

(5) Two kinds of angular correlations between the $\pi^\circ$ meson and neutron are defined as follows:

$$\Delta\phi=(\phi_{\pi^\circ}-\phi_n)/\sigma,$$
$$\Delta\theta=(\theta_0-\theta_n)/\sigma,$$
$$\sigma=d/R,$$

where $\phi_{\pi^\circ}$ and $\phi_n$ are azimuthal angles of the $\pi^\circ$ meson and neutron, respectively, $\theta_n$ is the measured angle of a recoiled neutron and $\theta_0$ is the predicted one from the scattering angle of the $\pi^\circ$ meson by using two body kinematics, and $d$ and $R$ are the half width of the neutron counter that is 50 mm and the distance between the target center and the front face of the neutron counter, respectively. These distributions are shown in Fig. III–3. The tail around $\Delta\theta\simeq 20$ is shown in Fig. III–3(b) and is due to the reaction of $\pi^-p\to\pi^\circ\Delta\to\pi^\circ\pi^\circ n$ ($\Delta$ event). This inelastic background was expected to be overlap with the elastic events. Fig. III–4 shows the correlation between a scattering angle of $\pi^\circ$ meson in the laboratory system ($\theta_L$) and $\Delta\theta$ after the $\Delta\phi$ cut was carried out at a momentum of 3.490 GeV/c. In this figure the upper band is due to the $\Delta$ event and the lower band is due to the elastic events which incldude the events from the bound protons in the target materials. As is seen, in the forward direction the inelastic events can be rejected perfectly by the $\Delta\theta$ cut, however, in the larger angular region than $\theta_L\sim 15^\circ$, two bands overlap each other. Taking into account of angular

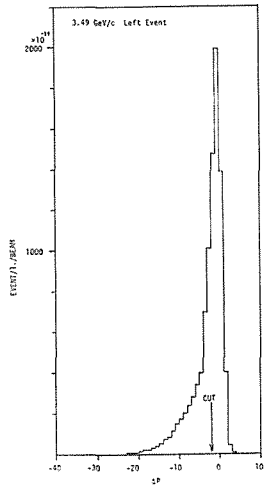


Fig. III–2

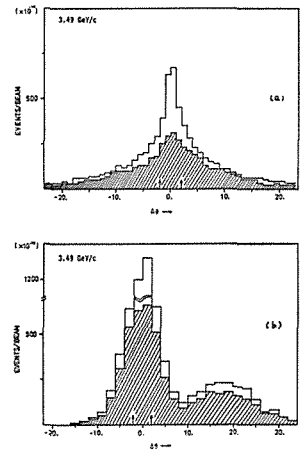


Fig. III–3

Fig. III–2 A typical $\Delta P$ distribution of the left event at the momentum of 3.49 GeV/c.

Fig. III–3 (a) A typical $\Delta\phi$ distribution of the left-right averaged event at the momentum of 3.49 GeV/c together with the background event from carbon run (shaded area) and candidate of the elastic events (indicated with arrows).

Fig. III–3 (b) A typical $\Delta\theta$ distribution for the same events.

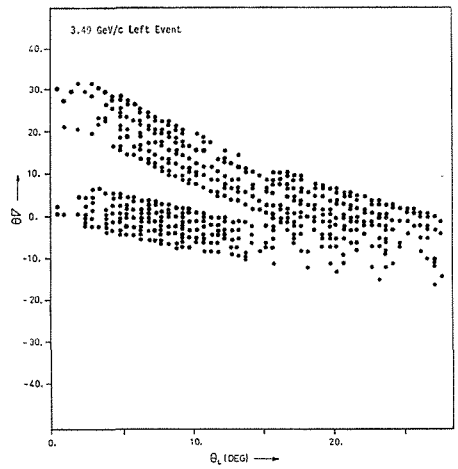


Fig. III–4 A typical $\Delta\theta$–$\theta_L$ correlation plot of the left events at the momentum 3.49 GeV/c.

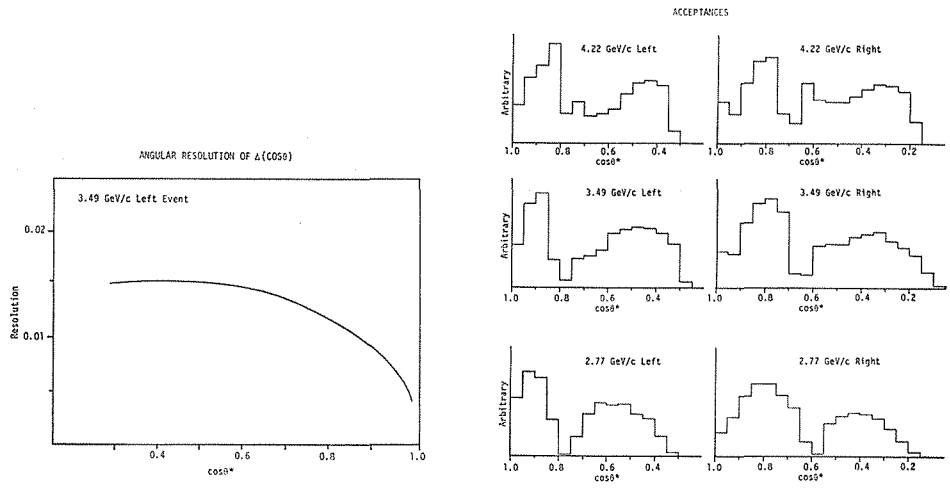


(a) (b)

Fig. III–5 (a) A resolution of the detection system calculated by the Monte-Carlo simulation.
Fig. III–5 (b) Angular acceptances of the detection system calculated by the Monte-Carlo simulation.

dependence of this inelastic events and yield of the upper band, the contamination due to $\Delta$ events in this angular region was estimated to be about 5% in average with respect to total events. Acceptance and angular resolutions were calculated with the Monte-Carlo simulation. They are shown in Fig. III–5.

(6) Finally, the momentum of $\pi^\circ$ meson in the center of mass system was evaluated. The typical momentum distribution is shown in Fig. III–6. The final candidates of charge exchange events, which had the momentum inside the region between 84% and 117% of the momentum evaluated from kinematics, were selected. As the result, remaining events amounted to 4~10% of collected events.

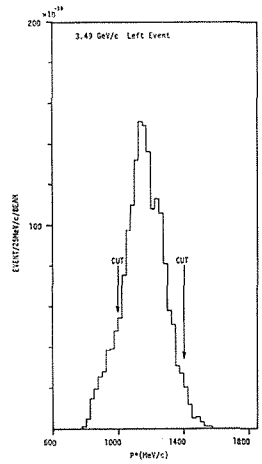


Fig. III–6 A typical distribution of the momentum in the center of mass system for the left events at the momentum of 3.49 GeV/c.

## C. Summary of Systematic Errors

Systematic errors of polarization parameters are mainly due to the following origins.

(1) An error arising from the background subtraction;
The background subtraction was performed by subtracting a yield obtained from carbon run from the yield obtained from target up (down) run at each angular bin. The error of this type was estimated to be 3%.

(2) An error arising from $\Delta$ event;
As is shown in Table III–2, this error has a main role in the larger angular

Table III–2. Contamination arising from $\Delta$ events is listed at both left and right events, where percentage is the ratio of the contribution of the $\Delta$ events to total yield after subtracting the contribution of bound protons and $\theta_L$ denotes a scattering angle in the laboratory frame.

Left Event

| $\theta_L$ (deg) | 2.770 GeV/c | 3.490 GeV/c | 4.220 GeV/c |
|---|---|---|---|
| 12.5~15.0 | — — | — — | 5 ± 2 % |
| 15.0~17.5 | — — | 7 ± 2 % | 7 ± 4 % |
| 17.5~20.0 | 3 ± 2 % | 5 ± 1 % | |
| 20.0~22.5 | 1 ± 1 % | 4 ± 1 % | 4 ± 2 % |
| 22.5~27.5 | 1 ± 1 % | 3 ± 1 % | |
| Average | 2 ± 2 % | 5 ± 3 % | 5 ± 3 % |

Right Event

| $\theta_L$ (deg) | 2.770 GeV/c | 3.490 GeV/c | 4.220 GeV/c |
|---|---|---|---|
| 15.0~17.5 | — — | — — | 1 ± 1 % |
| 17.5~20.0 | — — | 1 ± 1 % | 5 ± 2 % |
| 20.0~22.5 | — — | 2 ± 1 % | 8 ± 4 % |
| 22.5~27.5 | — — | 2 ± 1 % | — — |
| Average | — — | 2 ± 1 % | 5 ± 3 % |

region, and in those region it is estimated to be 5% in average.

(3) An error arising from the measurement of the target polarization; This error was estimated to be 5%, as is mentioned before.

## IV. Results and Conclusion

### A. Polarization Parameters

The polarization parameters for both left and right events are listed in Table IV–1 together with $\chi^2$ per data points at each momentum. And also averaged polarization parameters are listed both in $\cos\theta^*$ and $t$ range in Table IV–2.

The features of present data are summarized as follows.

(1) 2.770 GeV/c;

The first peak is seen at $\cos\theta^*>0.9$ ($-t<0.2$ (GeV/c)$^2$), and the second peak may be seen around $0.85>\cos\theta^*>0.75$ ($0.5>-t>0.3$ (GeV/c)$^2$). The negative broad dip is seen around $0.75>\cos\theta^*>0.6$ ($1.0>-t>0.5$ (GeV/c)$^2$).

Table IV–1. Polarization parameters for left and right event, where $P_L$ denotes the polarization parameters of the left event and $P_R$ denotes those of the right event. $\chi^2$'s per data point are also listed. Errors are statistics only.

| cos $\theta$ cm | 2.770 GeV/c | | 3.490 GeV/c | | 4.220 GeV/c | |
|---|---|---|---|---|---|---|
| | $P_L$ | $P_R$ | $P_L$ | $P_R$ | $P_L$ | $P_R$ |
| 0.97 ±0.02 | 0.33±0.08 | 0.09±0.10 | 0.01±0.10 | 0.23±0.09 | 0.14±0.14 | 0.51±0.11 |
| 0.925±0.025 | 0.25±0.06 | 0.26±0.08 | 0.19±0.07 | 0.43±0.11 | 0.24±0.11 | 0.15±0.23 |
| 0.875±0.025 | 0.20±0.09 | 0.03±0.10 | 0.57±0.12 | 0.40±0.23 | 0.48±0.25 | 0.52±0.24 |
| 0.825±0.025 | −0.01±0.23 | 0.17±0.19 | 0.09±0.67 | 0.37±0.24 | 0.97±0.80 | 0.03±0.41 |
| 0.75 ±0.05 | — — | 0.40±0.30 | −0.51±0.56 | −0.08±0.19 | −0.22±0.21 | 0.32±0.22 |
| 0.65 ±0.05 | −0.21±0.18 | −0.42±0.25 | 0.02±0.19 | 0.82±0.51 | 0.42±0.21 | 0.08±0.21 |
| 0.55 ±0.05 | 0.09±0.10 | −0.02±0.19 | 0.16±0.12 | 0.14±0.17 | 0.13±0.22 | 0.32±0.36 |
| 0.45 ±0.05 | 0.26±0.11 | 0.10±0.12 | −0.06±0.15 | −0.26±0.18 | 0.43±0.28 | 0.61±0.36 |
| 0.35 ±0.05 | 0.02±0.24 | 0.52±0.18 | −0.38±0.27 | 0.22±0.19 | −0.20±0.64 | −0.49±0.60 |
| 0.25 ±0.05 | — — | 0.25±0.16 | 0.97±1.92 | 0.43±0.34 | — — | — — |
| 0.15 ±0.05 | — — | — — | — — | 0.61±0.35 | — — | — — |
| $\chi^2$ per data point | 1.40 | | 1.24 | | 1.20 | |

Table IV–2. Averaged polarization parameters. Errors are statistics only.

| cos $\theta$ cm | $P_{lab}$=2.770 GeV/c $\sqrt{s}$=2.470 GeV/c | $P_{lab}$=3.490 GeV/c $\sqrt{s}$=2.730 GeV | $P_{lab}$=4.220 GeV/c $\sqrt{s}$=2.970 GeV |
|---|---|---|---|
| 0.97 ±0.02 | 0.24±0.06 | 0.14±0.06 | 0.46±0.09 |
| 0.925±0.025 | 0.25±0.05 | 0.25±0.06 | 0.22±0.10 |
| 0.875±0.025 | 0.12±0.07 | 0.54±0.11 | 0.50±0.17 |
| 0.825±0.025 | 0.10±0.15 | 0.33±0.23 | 0.22±0.36 |
| 0.75 ±0.05 | 0.40±0.30 | −0.13±0.18 | 0.03±0.15 |
| 0.65 ±0.05 | −0.28±0.14 | 0.12±0.18 | 0.25±0.15 |
| 0.55 ±0.05 | 0.06±0.09 | 0.16±0.10 | 0.18±0.19 |
| 0.45 ±0.05 | 0.19±0.08 | −0.14±0.12 | 0.45±0.26 |
| 0.35 ±0.05 | 0.33±0.15 | 0.02±0.16 | −0.36±0.44 |
| 0.25 ±0.05 | 0.25±0.16 | 0.43±0.34 | — — |
| 0.15 ±0.05 | — — | 0.61±0.35 | — — |

| $-t$ (GeV/c)$^2$ | $P_{lab}$=2.770 GeV/c $\sqrt{s}$=2.470 GeV | $P_{lab}$=3.490 GeV/c $\sqrt{s}$=2.730 GeV | $P_{lab}$=4.220 GeV/c $\sqrt{s}$=2.970 GeV |
|---|---|---|---|
| 0.07 ±0.03 | 0.28±0.07 | 0.20±0.10 | 0.39±0.11 |
| 0.15 ±0.05 | 0.24±0.05 | 0.14±0.96 | 0.27±0.11 |
| 0.25 ±0.05 | 0.12±0.07 | 0.39±0.09 | 0.26±0.13 |
| 0.35 ±0.05 | 0.21±0.12 | 0.51±0.13 | 0.14±0.21 |
| 0.5 ±0.1 | 0.21±0.21 | 0.36±0.17 | 0.69±0.20 |
| 0.7 ±0.1 | −0.35±0.23 | −0.18±0.21 | 0.14±0.31 |
| 0.9 ±0.1 | −0.13±0.10 | −0.02±0.16 | 0.14±0.19 |
| 1.1 ±0.1 | 0.20±0.09 | 0.10±0.19 | −0.07±0.21 |
| 1.3 ±0.1 | 0.23±0.10 | 0.19±0.12 | 0.27±0.19 |
| 1.5 ±0.1 | 0.34±0.19 | 0.02±0.13 | 0.54±0.34 |
| 1.7 ±0.1 | 0.31±0.18 | −0.27±0.16 | 0.00±0.20 |
| 1.9 ±0.1 | — — | 0.08±0.20 | 0.66±0.29 |
| 2.2 ±0.2 | — — | 0.52±0.26 | — — |

(2) 3.490 GeV/c;
The first peak mentioned above is obscure, however, the second peak is seen around the similar region as at 2.770 GeV/c.

(3) 4.220 GeV/c;
The first peak is again seen at the similar point as at 2.770 GeV/c. The second peak may be seen, although only one point is enhanced at $\cos\theta^* \simeq 0.8$ ($-t \simeq 0.5$ (GeV/c)$^2$).

### B. Comparison with CEX Experiment and PWA Prediction

The excitation of the previous measurement for polarization parameters at KEK (CEX experiment) are compared with the present results. In Fig. IV–1, the excitation of the polarization parameters at each angular bin is shown together with the prediction from K–H 78 analysis. The continuity (or consistency) of both measurements seem to be good at all angular bins, however, the prediction behaves somewhat differently from data except at forward angle of $\cos\theta^* > 0.85$.

In Fig. IV–2 the comparison between present data and the prediction from K–H 78 analysis again. The prominent feature is that at the momentum 2.77 GeV/c, both the present data and the prediction suggest that there seems to exist highly enhanced peak at $\cos\theta^* \simeq 0.8$. However, overall agreement becomes poor as the momentum increase but one must note the momentum difference between present data and the prediction.

In Fig. IV–3, the comparison between present data and the results at ANL is shown except at 4.22 GeV/c where no data exist. The agreement is very good, although there seems to exist some different behavior in the region of $|t| > 0.6$ (GeV/c)$^2$ at 3.49 GeV/c.

### C. Comparison with a Regge Model

As menttioned before, a simple $\rho$- exchange model for charge exchange scattering failed in explaining the non-zero polarizations at forward direction. To explain those non-zero polarizations, there proposed many attempts so far. Here, the analysis based on the secondary trajectory $\rho'$ is discussed.

From data at low energy, a Regge amplitude can be determined in terms of finite energy sum rule (FESR). FESR for any moment $S_n$ is expressed as follows[4].

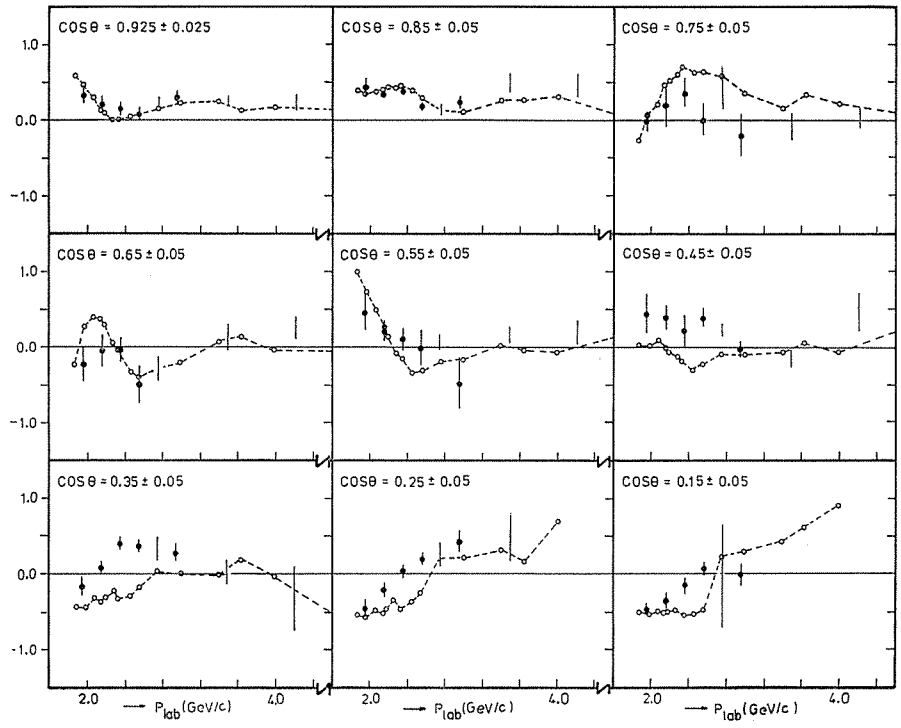


Fig. IV–1 An excitation of the polarization parameters in each angular bin. Where ⊕ represents the CEX experiment, | represents the present experiment and dashed lines represent the K–H 78 prediction.

$$S_n \equiv (1/N)^{n+1} \int_0^N \nu^n \,\mathrm{Im}\, F \mathrm{d}\nu = \sum_\alpha \beta N^\alpha / (\alpha+n+1)\Gamma(\alpha+1)$$
$$\nu = (s-u)/2M$$

where $F$ denotes crossing odd amplitude from phase shift analysis, $\beta$ denotes residue function, $\alpha$ denotes Regge trajectory, $M$ denotes nucleon mass and $s$ and $u$ denote Mandelstam variables. A Regge amplitude $R$ is defined as

$$R = \beta(1-e^{-i\pi\alpha})\nu^\alpha / \sin \pi\alpha\Gamma(\alpha+1)$$

In terms of $S_n$, $\alpha$ is determined, e.g., for single trajectory as follows:

$$S_n/S_m = (\alpha+m+1)/(\alpha+n+1)$$

and $\beta$ is calculated from $S_n$ with $\alpha$ determined above. Dolen et. al[4]. suggested the possibility of the second trajectory $\rho'$ by analysing $\pi N$ data combined with FESR mentioned above, in which case FESR is expressed as:

$$(S_1 - \beta N^{\alpha-1}/(\alpha+1)\Gamma(\alpha+1))/(S_3 - \beta N^{\alpha-1}/(\alpha+3)\Gamma(\alpha+1))$$
$$= (\alpha'+3)/(\alpha'+1)$$

where $\alpha$ and $\beta$ denote trajectory and residue of $\rho$, and $\alpha'$ denotes $\rho'$ trajectory.

Barger and Phillips extended FESR for any moment to continuous moments and

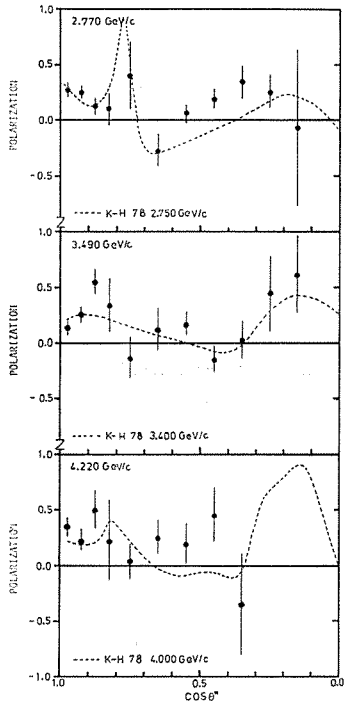


Fig. IV–2

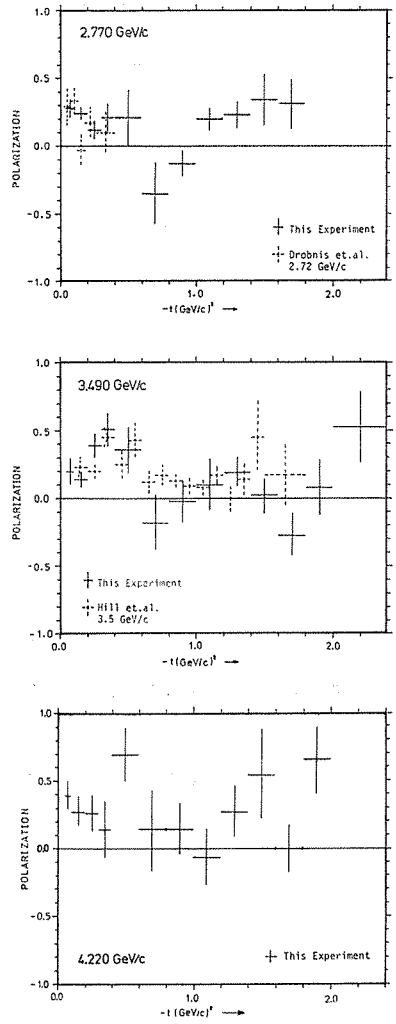


Fig. IV–3

Fig. IV–2 A comparison between the present data and K–H 78 prediction.
Fig. IV–3 A comparison between the present data and the data measured at ANL. Where + represents the present data and ⊹ represents the data of ANL. At the momentum 4.22 GeV/c, there exist no data except present one.

in terms of Regge trajectory. They analysed $\pi N$ data in the $t$ range up to $-2$ (GeV/c)$^2$ by introducing $\rho'$, $P'$ and $P''$ in addition to $\rho$ and $P$[3]. The results of their two analyses (B–P 69 and B–P 74) are shown in Fig. IV–4 together with the present data and CEX data, where dashed lines represent the B–P 69 analysis and solid lines represent the B–P 74 analysis.

For the differential cross section data (from CEX mefisurement) B–P 69 analysis well agree with data rather than B–P 74 analysis. For the polarization data (from CEX and the present measurement), both B–P 69 and B–P 74 analyses are in poor agreement with data.

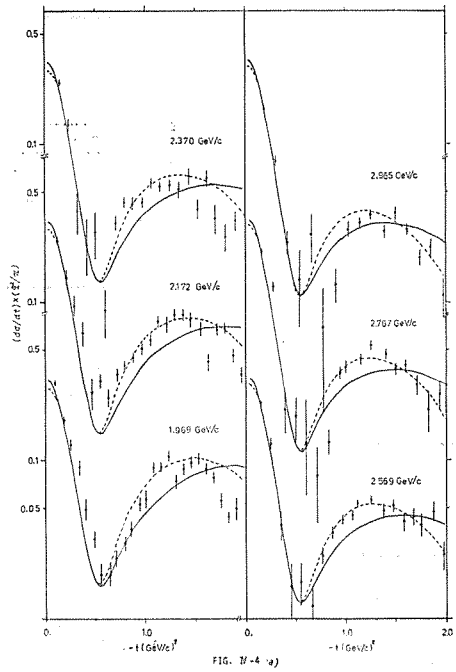


Fig. IV–4 (a) A comparison of the differential cross sections from ref. 10 with B–P 69 (dashed lines) and B–P 74 (solid lines) predictions.

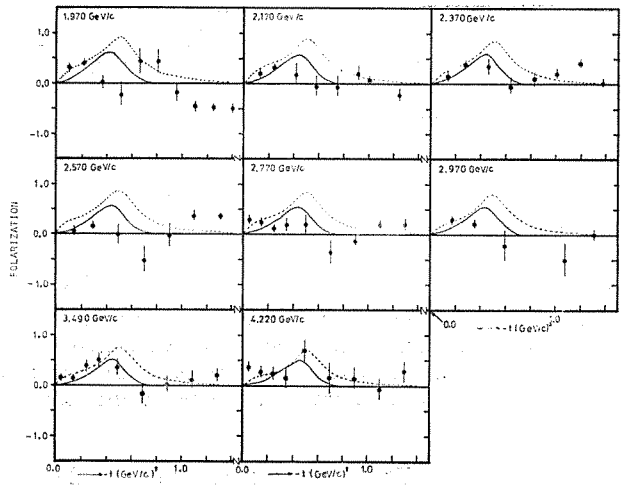


Fig. IV–4 (b) A comparison of the polarization parameters from ref. 11 and the present data with B–P 69 (dashed lines) and B–P 74 (solid lines) predictions.

In order to improve fits to the present energy region, data fitting in terms of their parametrization has been performed at three laboratory momenta of 2.77, 3.94 and 4.22 GeV/c in the $t$ range up to $-2$ (GeV/c)$^2$. The parametrization for invariant amplitudes $A'^-$ and $B^-$ are as follows:

$$A'^{-}=\sum -\gamma_i \nu(\nu_0^2-\nu^2)^{(\alpha_i-1)/2}$$
$$B^{-}=\sum -\beta_i(\nu_0^2-\nu^2)^{(\alpha_i-1)/2}$$
$$i=\rho,\ \rho',$$

where

$$\beta_\rho=-(a_1+a_2e^{b_1t})\Gamma(1-\alpha_\rho)\sin(\pi\alpha_\rho/2)$$
$$\beta_{\rho'}=-a_3te^{b_2t}$$
$$\gamma_\rho=a_4(1+a_5t)e^{b_3t}\Gamma(-\alpha_\rho)\sin(\pi\alpha_\rho/2)$$
$$\gamma_{\rho'}=-a_6t(1+a_7t)e^{b_4t},$$

which Barger and Phillips suggested as the best parametrization. Trajectories are adopted from their suggestion, i.e.,

$$\alpha_\rho=0.48+0.85t$$
$$\alpha_{\rho'}=0.3t.$$

All data used in the present analysis are 57 data points for differential cross sections[16] and 35 data points for polarization parameters (only including the present data), and they were fitted simultaneously by fitting program of SALS[17].

The results for 11 parameters of $a_1\sim a_7$ and $b_1\sim b_4$ are listed in Table IV–3 and the predictions are shown in Fig. IV–5. $\chi^2$ per degree of freedom is 4.0 for 92 data points. As is shown, good fits are obtained for differential cross sections. However, poor fits for polarization parameters remain, although fits are improved at forward angular region of $|t|<0.6$ (GeV/c)$^2$.

Table IV–3. Result of fitting parameters

| i | $a_i$ | $b_i$ |
|---|---|---|
| 1 | 19.4 | 1.51 |
| 2 | 108.4 | 6.81 |
| 3 | 541.2 | 3.22 |
| 4 | 5.1 | 22.20 |
| 5 | 6.2 | |
| 6 | 157.9 | |
| 7 | −19.7 | |

In Table IV–4, differential cross sections extrapolated to $t=0$ (GeV/c)$^2$ are compared with the prediction from the K–H 78 analysis[18], and a good agreement was obtained except at the momentum of 2.77 GeV/c.

Furthermore, $s$-channel helicity non-flip ($F^1_{++}$) and flip ($F^1_{+-}$) amplitudes extrapolated up to the momentum of 6 GeV/c are compared with the result of model independent analysis performed by Halzen and Michael (H–M 71)[19] in Fig. IV–6, where overall phase of those amplitudes are not taken into account. As is shown, a real part of $F^1_{++}$ is almost positive with having nearly zero at $t\simeq 0.35$ (GeV/c)$^2$, and an imaginary part has a first zero at $t\simeq -0.22$ (GeV/c)$^2$ which corresponds to cross over point. A real part of $F^1_{+-}$ is also almost positive with having nearly zero in the vicinity of $t\simeq -0.56$ (GeV/c)$^2$, and an imaginary part has a nonsense wrong signature zero at $t\simeq -0.56$ (GeV/c)$^2$, where a dip of differential cross section sites. The agreement with H–M 71 seems to be well for $F^1_{++}$ except at $|t|>0.4$ (GeV/c)$^2$ for a real part, however, there exist some discrepancies for $F^1_{+-}$.

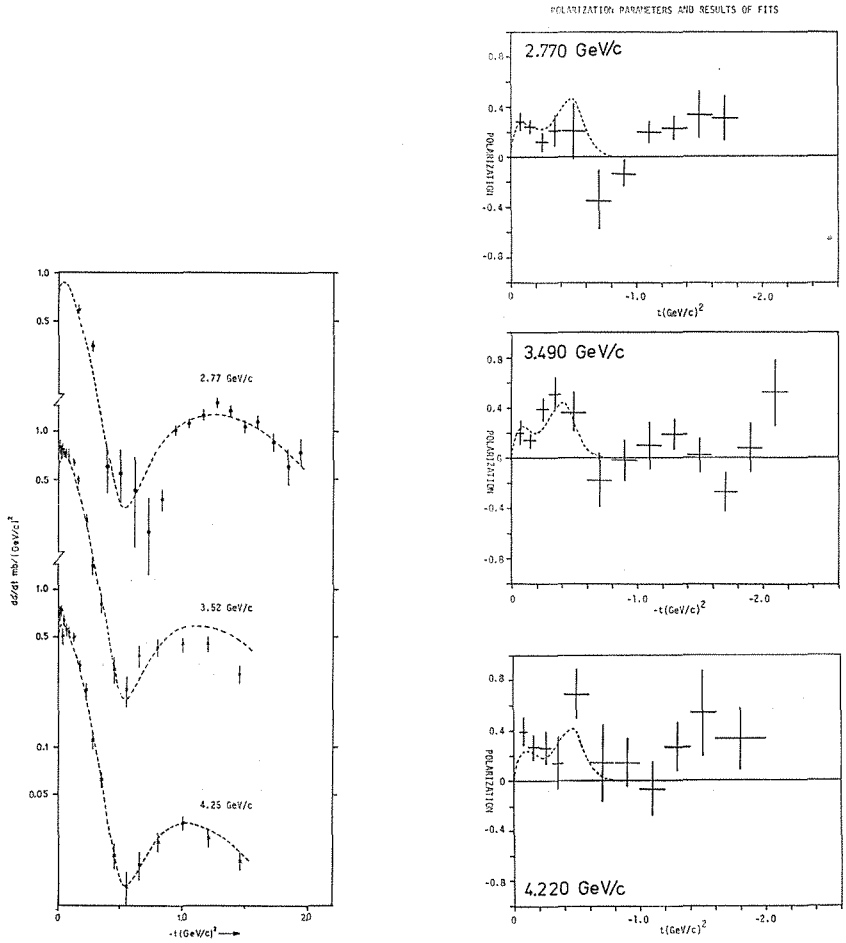


Fig. IV–5(a) The differential cross sections used in the present fitting and the results of the fits. Where ⊕ represents the data from ref. 10, ✳ represents the data from Yvert et. al. and dashed lines represent the results of the present fits.

Fig. IV–5(b) The polarization parameters of the present data and the results of the fits.

Table IV–4. Comparison between the fitting value and the K–H 78 prediction at $t=0$ (GeV/c)$^2$.

| $P_L$ (GeV/c) | $(d\sigma/dt)_{fit}$ | $(d\sigma/dt)_{KH}$ |
|---|---|---|
| 2.77 | 0.834 | 0.640 |
| 3.49 | 0.656 | 0.643 |
| 4.22 | 0.538 | 0.542 |
| 5.00† | 0.451 | 0.454 |

† At $P_L=5$ GeV/c, the differential cross section is extrapolated value in terms of fitting parameters determized from data fits.

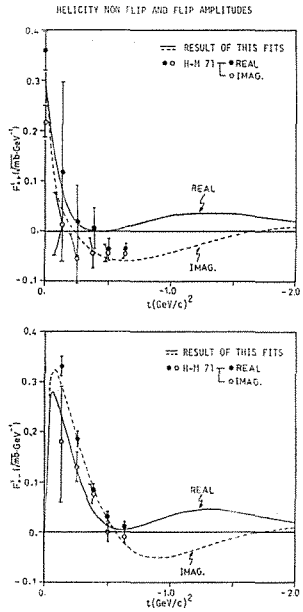


Fig. IV–6 The helicity non-flip and flip amplitudes of the results of the present fits and those of H–M 71. Where the solid and dashed lines represent the real and imaginary amplitudes of the present fits, respectively. ● and ○ represent the results of H–M 71.

Those features suggest that in order to improve the model, more terms, which may arise from Regge cuts and contribute in the larger $t$ region, must be required, and also a more complete set of $\pi N$ data at many momanta and large angular region must be accumulated for a model independent amplitude analysis as the test of the Regge model.

## D. Conclusion

The present results are in good agreement with those of ANL.

At the momentum of 2.77 GeV/c, the present data shows highly enhanced peak at $\cos\theta^* = 0.8$ as predicted from the K–H 78 analysis. However, overall agreement becomes poor as the momentum increases. It should be noted that there are some momentum differences between the prediction and the present data.

The prediction of a Regge model fail to reproduce the present data at larger angles, although the differential cross sections are in good agreement even at 2 GeV/c.

Those features of the forward data suggest as follows.

At low energy, polarization parameters (and of course, differential cross sections) at the forward direction are useful constraints for the phase shift analysis, therefore, a new phase shift analysis including present data is required.

At high energy, in order to improve the Regge models, more detailed behavior of the scattering amplitudes of the $s$ and $t$ dependence is required in terms of the model independent analysis like ref. 19, therefore, spin rotation parameters $A$ and $R$ in addition to differential cross sections and polarization parameters must be accumulated.

## ACKNOWLEDGEMENT

The auther would like to express his sincere thanks to Prof. K. Miyake and Prof. T. Nakamura for their continuous encouragement and guidance throughout this work. He is deeply grateful to Prof. M. Kobayashi, Dr. R. Kikuchi, Dr. Y. Hemmi, Dr. N. Sasao, Dr. T. Nakano, Dr. M. Daigo, Dr. M. Minowa, Dr. Y. Suzuki, Mr. S. Naito, Mr. M. Sakuda, Mr. M. Kobayashi and Mr. T. Ozaki for their advices and collaboration in carrying out this experiment.

Thanks are also due to Prof. A. Masaike, Prof. K. Morimoto, Dr. S. Hiramatsu, Dr. S. Isagawa and Mr. S. Ishimoto of the Polarized Target Group of KEK for thier efforts of constructing the polarized target system and for their valuable suggestions in operating the target.

He is indebted to most of the personnel at KEK, such as the members of the accelerator crew headed by Prof. Y. Kojima, for the stable operation of the proton synchrotron, those of the beam channel division headed by Prof. H. Hirabayashi for constructing and tuning the pion beam line, those of the counter division headed by Prof. Y. Nagashima for the assistance in preparing the electronics, the data handling dividsion headed by Prof. H. Takahashi for assistance in offline data analsysis and those of the workshop headed by Prof. T. Hongo for fabrication of the detectors and the mechanical instructions.

Finally, he would like to his sincere thanks to the members of the office of experimental planning and coordination headed by Prof. A. Kusumegi for their proper arrangement in efficient performance of the present experiment and their hospitality.

## Appendix A

From the CGLN formulation of $\pi N$ elastic scattering[20], $T$ matrix is expressed as follows:

$$T=A(\nu, t)+B(\nu, t)\not{Q}$$
$$Q_\mu=(q_\mu+q'_\mu)/2$$

where $q_\mu(q'_\mu)$ denotes four vector of the incident (scattered) pion and $\nu$ is defined as follows in terms of Mandelstam variables $s$, $t$ and $u$:

$$\nu=(s-u)/4M$$
$$\nu_0=\mu+t/4M$$

where $M$ denotes the nucleon mass and $\mu$ denotes the pion mass. And $\nu_0$ denotes the normal threshold. Let $\beta$ be the state of the final pion ($\beta=1, 2, 3$) and $\alpha$ be that of the initial pion. Then,

$$A_{\beta\alpha}=\delta_{\beta\alpha}A^{(+)}+[\tau_\beta, \tau_\alpha]A^{(-)}/2$$
$$B_{\beta\alpha}=\delta_{\beta\alpha}B^{(-)}+[\tau_\beta, \tau_\alpha]B^{(\pm)}/2$$

where $A^{(\pm)}$ and $B^{(\pm)}$ are iso-spin even(+) and odd(−) amplitudes, respectively. $\tau$ denotes iso-spin operator of the pion. In terms of those amplitudes, three reactions of $\pi N$ scattering are expressed as follows:

$$A(\pi^+p)=A^{(+)}-A^{(-)}$$

$$A(\pi^- p) = A^{(+)} + A^{(-)}$$
$$A(\pi^\circ n) = -\sqrt{2}A^{(-)}$$

and the similar forms for $B$. Furthermore, the invariant amplitude $A'$ is introduced:

$$A' = A + \nu B/(1 - t/4M^2)$$

The $s$-channel helicily non-flip ($F^I_{++}$) and flip ($F^I_{+-}$) amplitudes are also introduced for three reaction:

$$F_{++}(\pi^+ p) = F^0_{++} - F^1_{++}$$
$$F_{++}(\pi^- p) = F^0_{++} + F^1_{++}$$
$$F_{++}(\pi^\circ n) = -\sqrt{2}F^1_{++}$$

and the similar forms for $F_{+-}$, where 1 and 0 denotes total $t$-channel iso-spins.

The relation between $A'(B)$ and $F_{++}(F_{+-})$ are as follows:

$$4\sqrt{\pi}P_L F_{++} = \cos(\theta/2)(A' - t(M + \omega B/(4M^2 - t))$$
$$4\sqrt{\pi}P_L F_{+-} = \sin(\theta/2)(EA' - (4q^2 + t)MWB/(4M^2 - t)/M$$
$$E = \sqrt{(q^2 + M^2)}$$
$$\omega = \sqrt{(P_L^2 + \mu^2)}$$

where $P_L$ denotes incident pion laboratory momentum, $\theta$ denotes scattering angle in center of mass system and $W$ and $q$ denote the total energy and momentum in that system, respectively.

In terms of invariant amplitudes, a differential cross section ($d\sigma/dt$) and a polarization parameter ($Pd\sigma/dt$) are expressed as follows:

$$d\sigma/dt = (1/\pi s)(M/4q)^2((1 - t/4M^2)|A'|^2$$
$$-(t/4M^2)(4M^2P_L^2 + st)|B|^2/(4M^2 - t))$$
$$P(d\sigma/dt) = -\mathrm{Im}(A'B)\sin\theta/16\pi\sqrt{s}$$

Those formulation were used in the data fitting. The results on the fits are described in IV–C.

## Appendix B

The program for measuring the target polarization is described here. And the flow chart of the control program is shown in Fig. B–1. The essence is as follows.

At first, initial parameters are entered through the teletype. Main parameters are in the following.

(1) Sweep times (in the present case, 200 times for natural signals and 10 times for enhanced signals)
(2) Parameters used in the fitting procedure (the fitting region, the number of the data points and the number of the parameters)
(3) The kind of NMR signals (natural signals or enhanced signals)
(4) Functional switches which select the two modes:
One is the measuring mode and the other is the function generater mode where the computer only repeat the modulation of the radio frequencies. The latter mode is useful for the tuning of the measuring system.

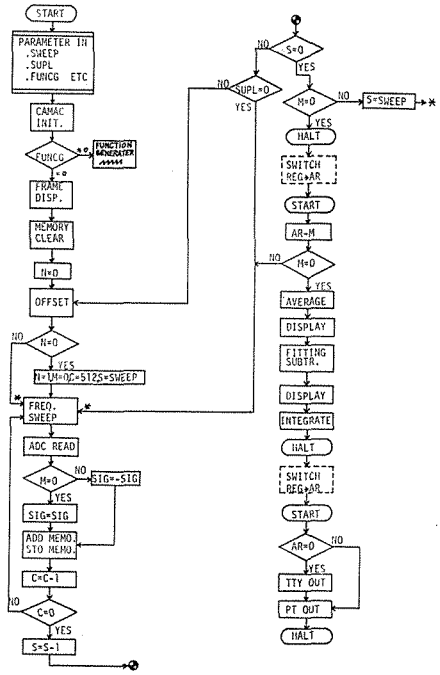


Fig. B–1 Flow chart of the ocntrol program for measuring the target polarization.

(5) Integrated natural signals combined with $P_0$.
(6) Other parameters are used for the auxiliary functions such as display parameters and the style for output (punching or printing).

Next, according to the selection switch for the NMR signals, the computer works in the two ways. In the case of natural signals, the computer waits after the first measuring ended, since one must remove the NMR signal so as to obtain only background signal. The background subtraction is performed automatically during the second sweep. And finally, chi-squared fitting is performed and the final signal is displayed. In the case of enhanced signals, the fitting is done immediately after the first measurement and the final signal is displayed.

## REFERENCES

1) P. Bonamy et al., Phys. Letters, **23** (1966) 51.
2) H. Harari, Phys. Rev. Letters, **26** (1971) 1400.
J. S. Loos and J. A. J. Matthews, Phys. Rev. **D6** (1972) 2463.
3) V. Barger and R. J. N. Phillips, Phys. Rev. **187** (1969) 2210.
V. Barger and R. J. N. Phillips, Phys. Letters **53B** (1974) 195.
4) R. Dolen et al., Phys. Rev., **166** (1968) 1768.
5) H. Naveret et al., Nucl. Phys. **B118** (1977) 475.
6) R. Ayed and P. Bareyre, Phys. Letters **50B** (1974) 1 (Rev. of Particle Properties).
7) G. Höhler et al., **TKP 78–11** and **TKP 78–12**.
8) R. E. Cutkosky et al., *Contributed paper to the 19th International Conference on High Energy Physics, Tokyo* (1978) No. 799.
9) J. L. Rosner, Phys. Report **11** (1974) 189.

R. J. Cashmore, *Proceeding of the 19th International Conference on High Energy Physics,* Tokyo (1978) p. 811.
10) Y. Suzuki, *Memoirs of the Faculty of Science, Kyoto University, Series A of Physics, Astrophysics, Geophysics and Chemistry Vol.* 36, (1981) 73.
11) M. Minowa, *Memoirs of the Faculty of Science, Kyoto University, Series A of Physics, Astrophysics, Geophysics and Chemistry Vol.* 36, (1981) 109.
12) McManigal et al., Phys. Rev., **148** (1966) 1280.
G. Cozzika et al., Phys. Rev., **164** (1967) 1672.
M. G. Albrow et al., Nucl. Phys. **B23** (1970) 445.
13) D. Drobnis et al., Phys. Rev. Letters **20** (1968) 274.
14) D. Hill et al., Phys. Rev. Letters, **30** (1973) 239.
15) N. Yamashita, *Memoirs of the Faculty of Science, Kyoto University, Series A of Physics, Astrophysics, Geophysics and Chemistry Vol.* 35 (1977) 35.
16) Ref. 10 for 2.77 GeV/c data.
Yvert et al., Prviate Communication (Gicomelli) (1968) for both 3.52 and 4.25 GeV/c.
17) T. Nakagawa and Y. Oyanagi, T–3–06 and T–3–07 (1979).
18) G. Höhler et al., **KfK 2735** (1979).
19) H. Halzen and C. Michael. Phys. Letters, **36B** (1971) 367.
20) C. G. Chew et al., Phys. Rev. **106** (1957) 1337.